Tropical Ocean Decadal Variability and Resonance of Planetary Wave Basin Modes. Part II: Numerical Study*

HAIJUN YANG

Department of Atmospheric Science, School of Physics, Peking University, Beijing, China

ZHENGYU LIU

Center for Climatic Research, University of Wisconsin—Madison, Madison, Wisconsin

QIONG ZHANG

LASG, Institute of Atmospheric Physics, Chinese Academy of Sciences, Beijing, China

(Manuscript received 11 February 2003, in final form 30 September 2003)

ABSTRACT

Oceanic response to stochastic wind forcing is studied in a tropical–extratropical basin using two shallow water models: a periodically forced model and a time-forward model. Consistent with theory, extratropical stochastic wind forces a decadal spectral peak in the tropical and eastern boundary ocean as a resonant response of the planetary wave basin mode. This resonant response is characterized by a rather uniform amplitude and phase in the equatorial and eastern boundary region. In comparison, away from the eastern boundary, the extratropical ocean is affected significantly by the local Ekman pumping forcing, with spectral peaks varying with location. A complex EOF (CEOF) analysis of the time-forward model simulation further suggests that these resonant responses are robust, and can be extracted as the leading CEOF modes. Thus, the resonance of the planetary wave basin mode gives a physically based guideline for the interpretation of decadal oceanic variability in the tropical–extratropical ocean.

1. Introduction

Considerable decadal climate variability has been observed over the tropical ocean (e.g., Zhang et al. 1997; Houghton and Tourre 1992). The origin of tropical decadal climate variability, however, remains poorly understood (e.g., Gu and Philander 1997; Kleeman et al. 1999; Barnett et al. 1999; Timmermann et al. 2003). Recently, using two classical theoretical models for a tropical–extratropical basin, Liu (2003, hereafter Part I) proposed that decadal spectral peaks can be generated in the tropical ocean due to the resonant excitation of planetary wave basin (PB) modes by extratropical stochastic wind. The primary spectral peak occurs at the period of the gravest PB mode, corresponding to a period of the cross-basin time of the planetary wave on the poleward boundary of the basin. These PB modes, first identified by Cessi and Louazel (2001), have been shown to be the slowest basin modes in a tropical–extratropical basin (Liu 2002; Yang and Liu 2003). In terms of classical equatorial wave dynamics on a finite equatorial β plane, these PB modes have been shown (Liu 2002) to be identical to the very low frequency scattering modes of Jin (2001).

This work extends the analytical theory of Part I to the full shallow water system using two numerical models: a periodically forced model and a time-forward model. The numerical results here confirm the idea of the dominant resonant response of the PB mode in the tropical and eastern boundary ocean. In the interior extratropical ocean, thermocline variability is contributed to significantly by the nonresonant response to local winds. The paper is arranged as follows. The models are introduced in section 2. Results from the periodically forced model and the the time-forward model are discussed in section 3 and 4, respectively. Further discussions are given in section 5 and a summary in section 6.

2. The models

The base model is the linear reduced-gravity shallow water model on an equatorial β plane in a closed basin:

* Center for Climatic Research Contribution Number 818.

Corresponding author address: Z. Liu, University of Wisconsin—Madison, 1225 W. Dayton St., Madison, WI 53706.
E-mail: zliu3@wisc.edu

$0 \le x \le L$, $Y_S \le y \le Y_N$. With a zonal wind stress τ, the time-forward shallow water model[1] is

$$\partial_t u - \beta y v = -g'\partial_x h + F + \mu(\partial_{xx}u + \partial_{yy}u) \quad (2.1a)$$

$$\partial_t v + \beta y u = -g'\partial_y h + \mu(\partial_{xx}v + \partial_{yy}v) \quad (2.1b)$$

$$\partial_t h + D(\partial_x u + \partial_y v) = 0, \quad (2.1c)$$

with a no-slip boundary condition. Here, $F = \tau/\rho D$ is the forcing and other parameters have their conventional meanings. This model can be simplified under a periodic forcing

$$\tau = \tau_0(y)e^{i\omega t}. \quad (2.2)$$

Now, the amplitude of the response satisfies a ''periodic'' model

$$i\omega u - \beta y v = -g'\partial_x h + F_0 + \mu(\partial_{xx}u + \partial_{yy}u) \quad (2.3a)$$

$$i\omega v + \beta y u = -g'\partial_y h + \mu(\partial_{xx}v + \partial_{yy}v) \quad (2.3b)$$

$$i\omega h + D(\partial_x u + \partial_y v) = 0, \quad (2.3c)$$

where $F_0 = \tau_0/\rho D$. Both model (2.1) and (2.3) will be solved numerically using finite differences (see Yang and Liu 2003 for detail). For comparison of the results, the same spatial finite-difference scheme (C grid) and resolution (dx = 100 km, dy = 100 km) are used in both models. The time-forward model also uses the leapfrog in time (dt = 1h). (Experiments show that the major conclusions are insensitive to the model resolution.) The periodic model can be used to study the oceanic response to a white noise forcing by assuming forcing amplitude τ_0 independent of frequency ω [as in (2.2)]. The periodic model provides a bridge between the theory and the time-forward model—a model more relevant to reality.

Typical model parameters are chosen as $\beta = 2 \times 10^{-11}$ m s^{-1}, D = 400 m, and $g' = 0.02$ m s^{-2} giving the gravity wave speed $c_0 = \sqrt{g'D} = 2.8$ m s^{-1}, and the equatorial deformation radius $L_D = (c_0/\beta)^{1/2} = 377$ km. Due to the limit of our computer memory for the matrix operation in model (2.3), we have used a basin of L = 3000 km and Y_N = 5000 km. For this basin, the cross-basin times of the equatorial Kelvin wave and the northern boundary planetary wave are, respectively,

$$T_{\mathrm{EK}} = L/c_0 \approx 12.5 \text{ days} \quad \text{and} \quad (2.4)$$

$$T_{\mathrm{P1}} = L/c_{\mathrm{PN}} \approx 6 \text{ yr}, \quad (2.5)$$

where $c_{\mathrm{PN}} = \beta(c_0/\beta Y_N)^2$ is the planetary wave speed on Y_N. For a realistic basin of the Pacific Ocean ($L \approx 10\,000$ km), $T_{\mathrm{PI}} \approx 18$ yr, that is, the planetary wave traveling time would be at the decadal time scale, consistent with the estimate based on the altimeter observation (Fu and Chelton 2001; Yang and Liu 2003). This decadal time scale is much longer than the time scale of the equatorial basin (EB) mode (Cane and Moore 1981), which is bounded by 4 times the Kelvin wave time (2.4) and is, therefore, at seasonal time scales. The Laplacian diffusion coefficient is chosen as $\mu = 2 \times 10^4$ m^2 s^{-1} here, corresponding to a Munk boundary layer width of 100 km. (We also used a linear drag damping. The results are not sensitive to the type of damping.)

In this work, we will only study the hemispherically symmetric response. Therefore, in the periodic model, a symmetric boundary condition is applied on the southern boundary at the equator $Y_S = 0$. In the time-forward model, both the basin ($Y_S = -Y_N$) and forcing are symmetric about the equator.

3. Results from the periodic model

As in Part I, for the periodic model, extratropical wind tends to force a decadal peak response in the tropical ocean due to the resonant PB modes, while equatorial wind tends to force a high frequency spectral peak due to the resonant EB modes. We first examine the oceanic response to a localized Gaussian wind patch centered at y_C:

$$\tau_0(y) = e^{-[(y-y_C)/l_y]^2}, \quad (3.1)$$

where $l_y = 5°$. With an equatorial wind patch ($y_C = 0$, Fig. 1c), the eastern boundary thermocline exhibits a distinct spectral peak at the frequency of

$$\omega_{\mathrm{EI}} = 2\pi/(4T_{\mathrm{EK}}), \quad (3.2)$$

on the equator (Fig. 1a, solid) and in the extratropics (Fig. 1b, solid). This frequency corresponds to the first EB mode, as seen in the eigenvalue spectrum of the EB modes (Fig. 1g). Therefore, this peak response on the eastern boundary, which is also apparent on the equator away from the eastern boundary (Fig. 1a, dash and dash-dot lines), reflects the resonant response of the first EB mode. In the extratropical interior ocean, however, the resonant peak of the EB mode disappears, with a significant reduction of the overall variability (Fig. 1b, dash and dash-dot lines). This is expected because the EB mode is trapped near the equator (Cane an Moore 1981; Yang an Liu 2003).

In contrast, with extratropical wind ($y_C = 30°$, Fig. 1f), the dominant response along the entire equator (Fig. 1d) and the extratropical eastern boundary (Fig. 1e, solid line) exhibit a peak response at the frequency of the first PB mode

$$\omega_{\mathrm{P1}} = 2\pi/T_{\mathrm{P1}}, \quad (3.3)$$

corresponding to a period of the cross-basin time of the planetary wave on Y_N. However, in the extratropical interior ocean, this resonant peak disappears (Fig. 1e, dash and dash-dot lines); instead, the spectrum ten to be red, because it is dominated by the local Ekman pumping forcing (Frankignoul et al. 1997), instead of eastern boundary thermocline variability. Compared with the inviscid theory for equatorial waves (Part I;

[1] The time-forward model here is actually solved using the spherical coordinate version of (2.1).

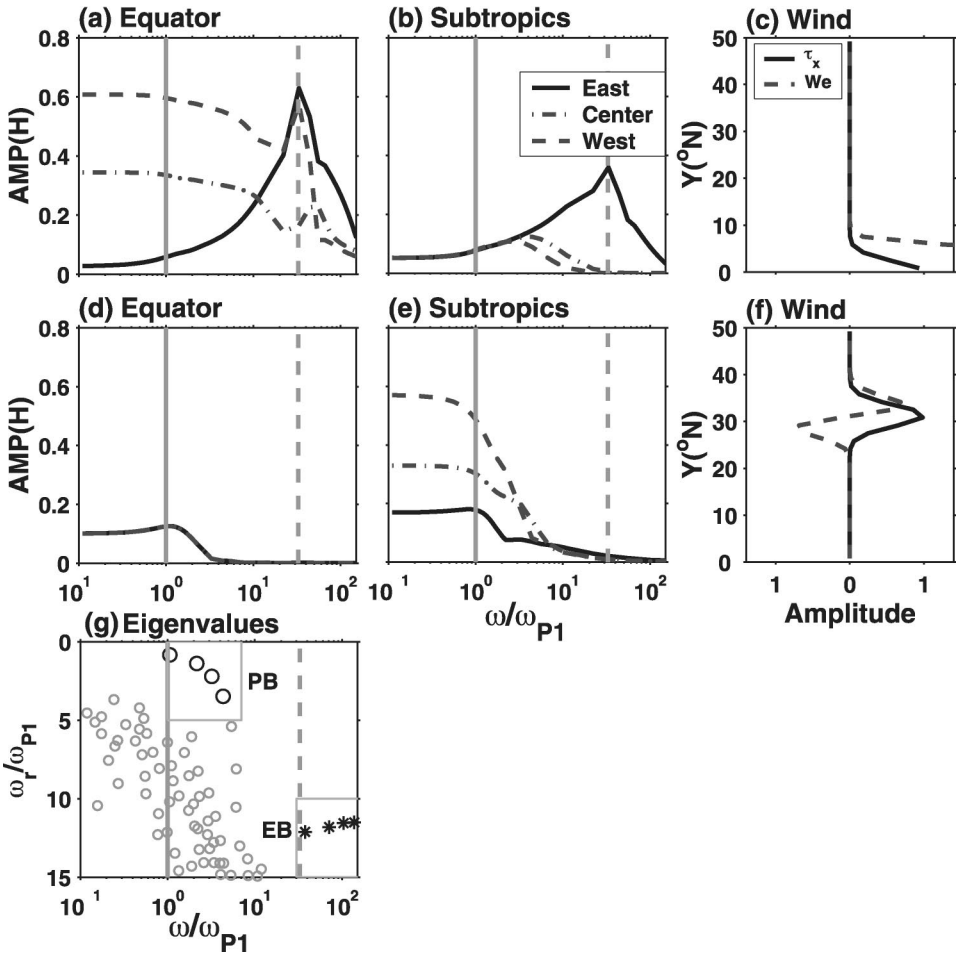

FIG. 1. The amplitude spectra of h forced by a white noise wind (2.2) in the periodic model (2.3). For a Gaussian equatorial wind patch as shown in (c) [$y_C = 0$ in (3)], the spectra are shown along (a) the equatorial ($y = 0$) and (b) a subtropical ($y = 25°$) latitude at the eastern boundary ($x = 30°$, solid line), the central basin ($x = 15°$, dash-dot line), and western boundary (outside the boundary layer at $x = 5°$, dash). (d) and (e) The same as (a) and (b), but for the Gaussian wind patch in the extratropics ($y_C = 30°$) as shown in (f). (g) For reference, the eigenvalue spectrum of the free modes are also plotted (Yang and Liu 2003), where the leading PB modes and EB modes are marked in heavy circles and asterisks, respectively. The frequency in the x axis is normalized by ω_{P1} in (3.3); the vertical gray lines mark the frequencies of the first PB (solid) and EB ($\omega_{E1}/\omega_{P1} = 44$, dashed) line modes; h (here and in following figures) is normalized by $\tau_0 L/\rho c_0^2$ with τ_0 being the amplitude of the zonal wind stress. The corresponding Ekman pumping is also plotted as the dashed line in (c) and (f).

Fig. 1), the magnitude of the resonant peak on the equator is reduced by 10 times for the high-frequency EB mode under the equatorial wind (Figs. 1a,b), but remains about the same at low frequencies for the resonant PB mode under the equatratropical wind (Figs. 1d,e). The much more severe reduction of the EB mode response in our numerical model here occurs because the smaller scale of the EB mode makes it more vulnerable to dissipation.

Similar to Part I (their Fig. 3), the generation of the resonant PB mode is seen more clearly by examining the spectral response (Fig. 2) forced by a wind patch (3.1) that shifts systematically poleward. On the equator (Figs. 2a,b), the most striking feature is the emergence of a dominant resonant peak toward the first PB mode when the wind shifts toward the extratropics (for about $y_C > 10°$). The resonant response is rather uniform along the equator, as seen in the similar spectra at the eastern boundary (Fig. 2a) and the central basin (Fig. 2b). In contrast, equatorial wind (say, $y_C < 5°$) forces a spectrum that increases toward higher frequencies (Figs. 2a,b), due to the resonance of the first EB mode (as in Fig. 1a).

In the extratropics (e.g., on $y = 25°$), the interior ocean (Fig. 2d) is not dominated by the resonant PB modes, in contrast to the eastern boundary (Fig. 2c) and the Tropics (Figs. 2a,b). In the central extratropical basin (Fig. 2d), only a weak resonance peak appears as a

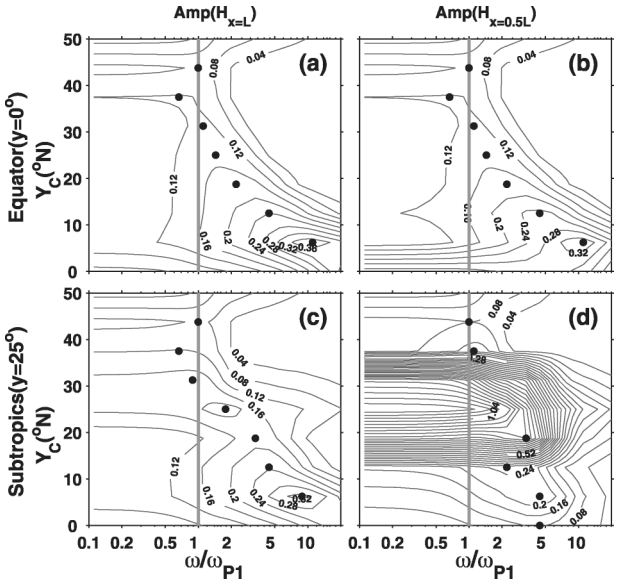

FIG. 2. The amplitude spectra of the periodic model on the equator $y = 0°$ at (a) the eastern boundary and (b) central basin as a function of the central latitude of the Gaussian wind patch y_C. (c), (d) The same as (a) and (b), but in the subtropics on $y = 25°$.

nonlocal response to wind in the south ($y_c < 15°$) and north ($y_c > 35°$). This weak resonant response, as will be seen later, is overwhelmed by the strong direct response to the local Ekman pumping on the same latitude ($15° < y_c < 35°$),[2] which tends to generate a red spectrum (Frankignoul et al. 1997).

With a basinwide extratropical wind of a sine profile (Fig. 3a), the power spectrum peaks at the first PB moe uniformly along the equator (Fig. 3c), because of the absence of wind on the equator. In the extratropics (Fig. 3b), the eastern boundary exhibits the same decadal peak as on the equator, while the central and western oceans do not peak at the first PB mode (Cessi and Louazel 2001; Part I)—all in good agreement with Part I (their Fig. 5g). The differences of the spectra between the equatorial and extratropical regions are seen more clearly in the magnitude and frequency of the primary (or maximum) spectral peak. Along the eastern boundary and the equator, the amplitude is rather uniform (Fig. 4a) and the frequency is near the first PB mode ($\omega \approx 0.8\ \omega_{P1}$), demonstrating clearly the resonance of the first PB mode there. In the off-equatorial region ($y > 15°$), the amplitude first decreases slightly toward the central basin and then increases significantly toward the northwestern corner (Fig. 4a), while the frequency first increases abruptly more than 3 times along a narrow front an then decreases smoothly toward the northwest (Fig. 4b). In the interior extratropical ocean, low-frequency spectral peaks do emerge (Cessi and Louazel 2001; also see Fig. 3b);[3] but, this peak response differes from the resonant response on the equator, which has a single frequency of primary peak; it also differs from the locally forced thermocline response in the absence of eastern boundary variability, which has a red spectrum toward the low-frequency limit (Frankignoul et al. 1997). The extratropical response is due to the significant contribution of the local Ekman pumping effect $\int_L^x w_e/c_p(y)\ dx$, which increases westward due to the accumulation of the Ekman pumping by the planetary wave, and which is inversely proportional to the speed $c_p(y)$. Toward the equator [$y \to 0$, $c_p(y) = \beta(c_0/\beta y)^2 \to \infty$], the wave speed increases to infinity, resulting in a diminishing local Ekman pumping effect and, in turn, leaving a dominant effect of the resonant PB mode there.

Finally, under the periodic forcing of the frequency of the first PB mode, the amplitude (Fig. 5a) is largely uniform along the equator and the eastern boundary and increases toward the northwestern corner, while the phase (Fig. 5b) shows a westward propagation with the phase line roughly proportional to the planetary wave speed. The patterns of amplitude and phase are in good agreement with the theory (Figs. 6a,b of Part I) and have some similarity to the eigenfunction of the first PB mode (Figs. 5c,d).

4. Results from the time-forward model

The time-forward model (2.1) will be forced by a stochastic zonal wind:

$$\tau = \tau_0(y)W(t), \tag{4.1}$$

where $\tau_0(y)$ is the latitudinal wind profile and $W(t)$ is a random time series of Gaussian distribution. First, we show that the result from the time-forward model is consistent with the periodic model. Ensemble experiments with 25 members are performed with an extratropical sine wind profile (Fig. 3a). Figure 6 shows the amplitude spectra of h in the extratropics (Figs. 6a–c) and on the equator (Figs. 6d–f) for individual experiments (thin gray lines) and the average spectrum (heavy black line). These spectra are in good agreement with Figs. 3b and 3c in the periodic model, with the resonant first PB mode dominant on the equator (Figs. 6d–f) and the eastern boundary (Fig. 6c), but not in the extratropical interior ocean (Figs. 6b,a). The distribution of the amplitude and frequency of the primary peak for the averaged spectrum (Fig. 7) also shows a general agreement with the periodic model (Fig. 4). It is interesting that, in spite of the clear resonant dynamics, the resonant peak of the first PB mode in the equatorial and

[2] The Gaussian patch has a finite width such that the Ekman pumping forces directly on $y = 25°$ when $15° < y_c < 35°$.

[3] The primary peak frequency decreases to smaller than that of the first PB mode toward the northwestern corner. Therefore, there are also regions in the extratropical interior ocean where the primary peak is close to the first PB mode. These peaks, however, are not caused by resonance of the PB mode.

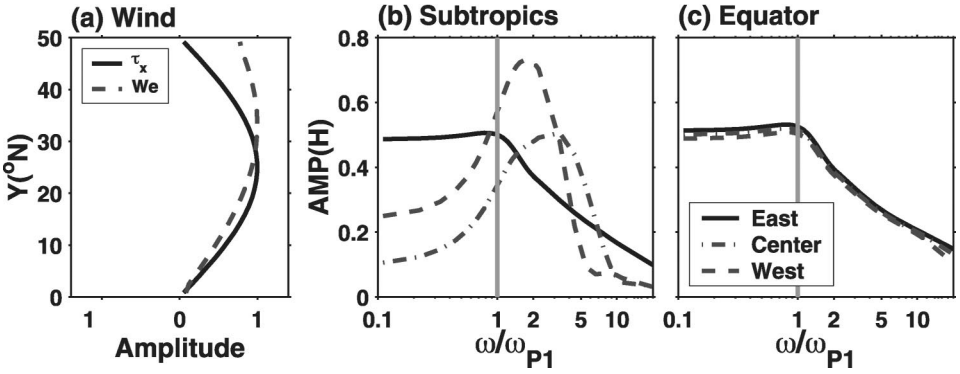

FIG. 3. The amplitude spectra of the periodic model (c) on the equator and (b) in the subtropics $y = 25°$, at the eastern boundary (solid line), central basin (dash-dot line), and near the western boundary ($x = 5°$, dash) forced by a white noise wind of the sine profile shown in (a).

eastern boundary region does not pass the 90% confidence level against a red noise spectrum.

The presence of the PB mode is critical for the resonance responses above. To demonstrate this, heavy damping is applied artificially along the western boundary to suppress the reflection of coastal Kelvin waves and, in turn, the PB modes in both models, as in Yang and Liu (2003) [The absence of the PB modes are confirmed in the eigenvalue calculation (not shown)]. Both models are then forced by the same stochastic forcing of the sine profile Fig. 3a. Now, the variability virtually disappears on the equator (Figs. 8b,d) and eastern boundary (Figs. 8a,c, solid lines). Furthermore, the spectra remain virtually white in the low-frequency range, as with the forcing, with the resonant peaks [in Figs. 3c, Fig. 3b (solid line), and Figs. 6c–f] disappearing completely. The extratropical interior ocean has a red spectrum with the amplitude increasing westward (Figs. 8a,c, dash and dash-dot lines), as does the response purely forced by local Ekman pumping in the absence of thermocline variability on the eastern boundary (Frankignoul et al. 1997).

The regional spectra (in Fig. 6) contain the resonant responses of all the modes as well as the purely forced response. It is generally difficult to separate the modular response without resorting to more complicated dynamic analysis. As a simple and practical statistic analysis, here, the complex EOF (CEOF; Horel 1984) analysis is applied to the thermocline variability of each individual ensemble member. The CEOF analysis are almost the same among all the different members, with the first three CEOF modes explaining about 66%, 21%, and 8% of the variance. CEOF1 is dominated by the resonance of the first PB mode. The real part (Fig. 9a1) is rather uniform in the equatorial/eastern boundary region and exhibits a wavenumber-1 structure along the northern

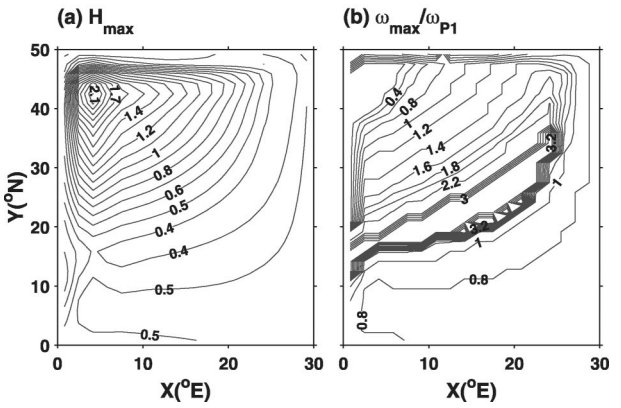

FIG. 4. (a) Magnitude and (b) frequency (normalized by ω_{P1}) at the maximum peak of the power spectra forced by the white noise wind of the sine profile in Fig. 3a in the periodic model.

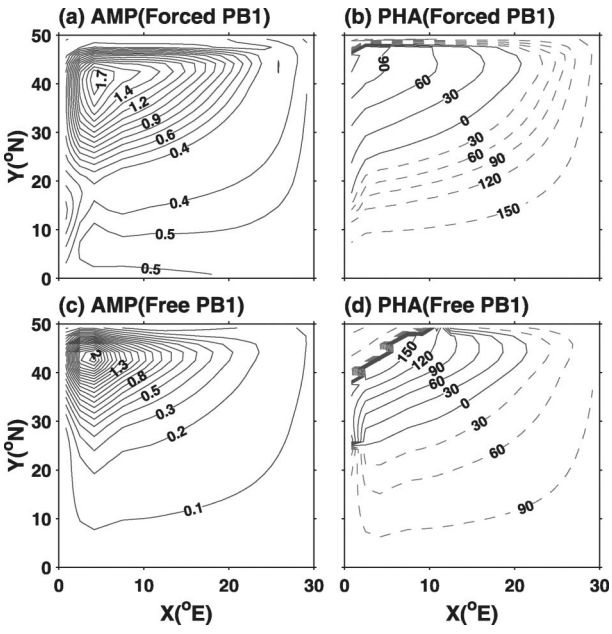

FIG. 5. (a) Amplitude and (b) phase of the forced response under the sine wind profile (Fig. 3a) of the frequency ω_{P1} in the periodic model. (c), (d) The amplitude and phase of the eigenfunction of the first PB mode, respectively.

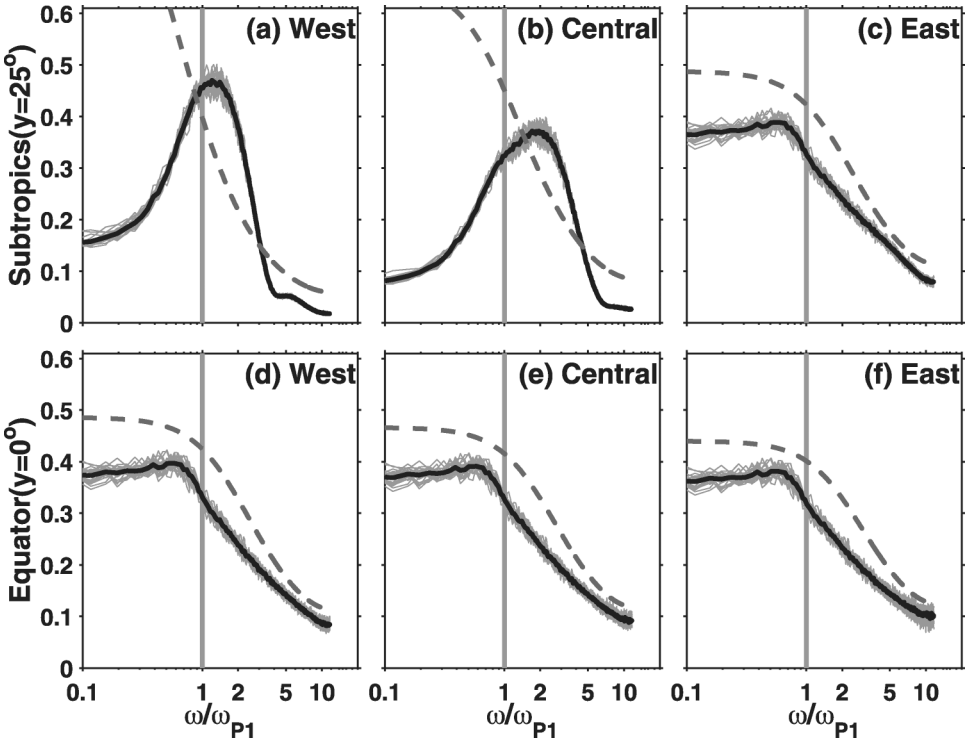

FIG. 6. The regional amplitude spectra of the time-forward model under a stochastic wind of the sine profile (Fig. 3a). The thin gray lines are the spectra of the 25 ensembles (each is integrated for 300 yr with the 3-month average data used for analysis) and the black line is the average of the 25 ensemble members. (a), (b), (c) The spectra near the western boundary ($x = 5°$), at the central basin and the eastern boundary in the extratropics ($y = 25°$). (d), (e), (f) The same as (a), (b), and (c), respectively, but on the equator.

boundary; this pattern is shifted westward about 90° in the imaginary part (Fig. 9a2); the amplitude (Fig. 9a3) and phase (Fig. 9a4) are uniform along the equator/eastern boundary, and show a westward propagation in the extratropics. Overall, CEOF1 is reminiscent of the first PB mode (Figs. 5c,d) and resembles closely the response forced at the frequency $\omega = \omega_{PI}$ (Figs. 5a,b). Most importantly, the spectra of CEOF1 (the time coefficients of the real part; Fig. 9a5) show a pronounced peak of the first PB mode. These spectral peaks in most ensemble members are significant at the 90% level, much more significant than those for regional time series on the equator (Figs. 6d–f). The message is that CEOF is capable of extracting the dominant signal of a resonant physical mode. This is not an obvious result, considering that the shallow water system is not self-adjoint (North 1984).

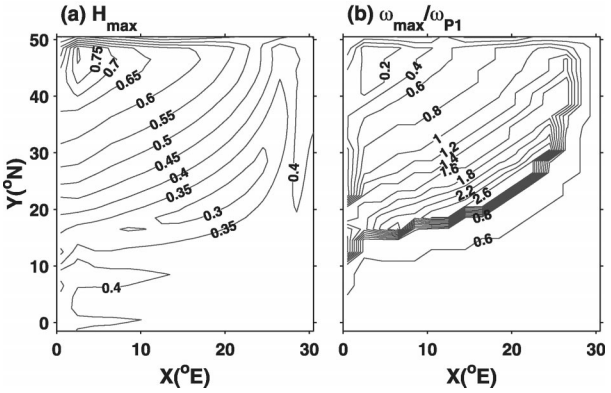

FIG. 7. The same as Fig. 4, but for the average spectrum of the 25 ensemble members in the time-forward model.

The CEOF analysis also seems to be capable of extracting more subtle physical modes. For example, CEOF3 (Fig. 9c) appears to be dominated by the resonance of the second PB mode, as characterized by rather uniform response along the equator and a wavenumber-2 structure on the northern boundary (Figs. 9c1–4) (Cessi and Louazel 2001; Liu 2002), and most clearly, a pronounced spectral peak of the second PB mode (Fig. 9c5). This weak signal of the second PB mode is difficult to detect in the regional power spectra in Fig. 6.

The pattern of CEOF2 (Fig. 9b1–b4) appears to lie between the first and second PB modes. Yet, its coefficient (Fig. 9b5) exhibits predominantly a red spectrum, with no distinguished peak in the low-frequency range. This mode, we speculate, is not completely unphysical. This mode contributes substantially to the power spectrum in the frequency range lower than the first PB mode and may explain why the regional time series on the

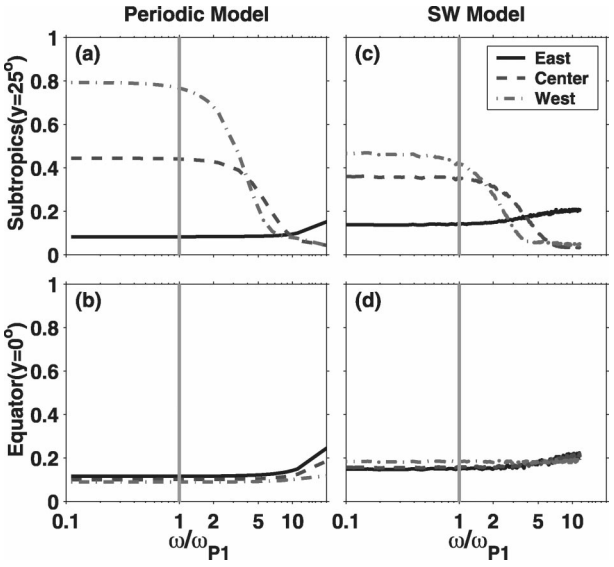

FIG. 8. The amplitude spectra under a white noise sine profile wind with a heavy linear damping in all the three equations within the western boundary. (a), (b) The periodic model in the extratropics ($y = 25°$) and the equator, respectively (solid line at the eastern boundary, dashed line at the central basin, and dash-dot line near the western boundary at $x = 5°$). (c), (d) The same as (a) and (b), but in the time-forward model for the average of a 10-member ensemble. All the experiments are integrated for 300 yr and the 3-month average data are used for analysis.

equator (Figs. 6d–f) has more power at the low-frequency end than that of CEOF1 (Fig. 9a5). Perhaps, CEOF2 represents predominantly the forced response to local Ekman pumping (Frankignoul et al. 1997), which is independent of the PB mode. If true, the less pronounced peak at the first PB mode in the regional time series (Figs. 6d–f) than in CEOF1 (Fig. 9a5) may be interpreted as being distorted by the local Ekman pumping effect in the extratropics. In any case, the extraction of the resonant PB mode response by the leading CEOF modes suggests that the resonance of PB mode is robust and, in principle, can be detected in a finite time series like the observed climate data or a coupled model.

5. Discussion

The spectrum of the oceanic response depends on the wind profile, because of the competition between the extratropical and tropical winds. The former favors the resonant PB mode while the latter favors the EB mode (Fig. 1). With a cosine wind profile (Fig. 10a) that has an equal but opposite wind stress on the equator and the northern boundary, the results obtained in the periodical model show that the spectra in the eastern and central equatorial regions have a primary resonant peak at the first EB mode and a secondary resonant peak at the first PB mode (Fig. 10c, solid and dashed lines). This differs from the sine wind forcing (Fig. 3a), which has no wind on the equator and, therefore, only forces the resonant peak at the first PB mode (Fig. 3c). This double-peak spectrum is also found along the eastern boundary in the extratropics (Fig. 10b, solid). In the central and western extratropical ocean (Fig. 10b, dash and dash-dot lines), however, the spectral peaks are similar to the case of sine wind (Fig. 3b), with no resonance at the first PB mode. Therefore, the spectrum of the response is not very sensitive to the wind pattern in the extratropical interior ocean.

The amplitude (Fig. 11a) and frequency (Fig. 11b) of the primary peak differ from those under the sine wind (Fig. 4) mostly in the equatorial region, as indicated by the high-frequency primary resonance near the first EB mode ($\omega_{EI}/\omega_{PI} = 44$) there. In addition, the amplitude reaches a minimum in the central equatorial region (Fig. 11a), reminiscent of the node point of the first EB mode there (Cane and Moore 1981; Yang and Liu 2003). In the interior extratropical ocean, however, the frequency of the primary peak increases smoothly toward the northwest (Fig. 11b), similar to the case of the sine wind forcing (Fig. 4b), because the response here is contributed to mostly by the local response. To focus on low-frequency responses, the analysis can be carried for the ''low pass'' data in the frequency range $\omega < 6\omega_{P1}$. Now the amplitude (Fig. 11c) has a minimum in the central equatorial region and the overall pattern is similar to that forced by the periodic forcing of the frequency of the first PB mode (not shown, see the theory in Fig. 6c of Part I). The frequency of the primary peak (Fig. 11d) is now dominated by that of the first PB mode in the central-eastern equator/eastern boundary region. This suggests that a low-pass filter is useful for extracting the PB mode response.

With the cosine wind profile shifted poleward by 12° (Fig. 12a), the equatorial wind weakens while the subtropical wind strengthens, relative to the cosine wind (Fig. 10a). The resonant PB mode spectral peak becomes clearer (Figs. 12b,c) along the equator/eastern boundary, as expected. The amplitude (Fig. 13a) and frequency (Fig. 13b) of the primary spectral peak is dominated by the first PB mode in the central equatorial and eastern boundary region, with an overall amplitude increasing toward the northwestern corner, somewhat similar to the case of the sine wind (Figs. 4a,b). Finally, in the low-frequency range of $\omega < 6\omega_{P1}$, the amplitude (Fig. 13c) and frequency (Fig. 13d) of the primary peak become even more similar to the case of the sine wind (Figs. 4c and 4d), indicating the dominance of the low-frequency variability by the extratropical wind.

Similar results can be obtained in the time-forward model. Figure 14 presents the regional spectra forced by the stochastic wind of the shifted cosine profile (Fig. 12a) for a 25-member ensemble. The regional spectra resemble closely that of the periodic model in Figs. 12b and 12c. In particular, the resonance peak of the first EB mode is always significant at the 90% level, while the resonant peak of the first PB mode is significant at

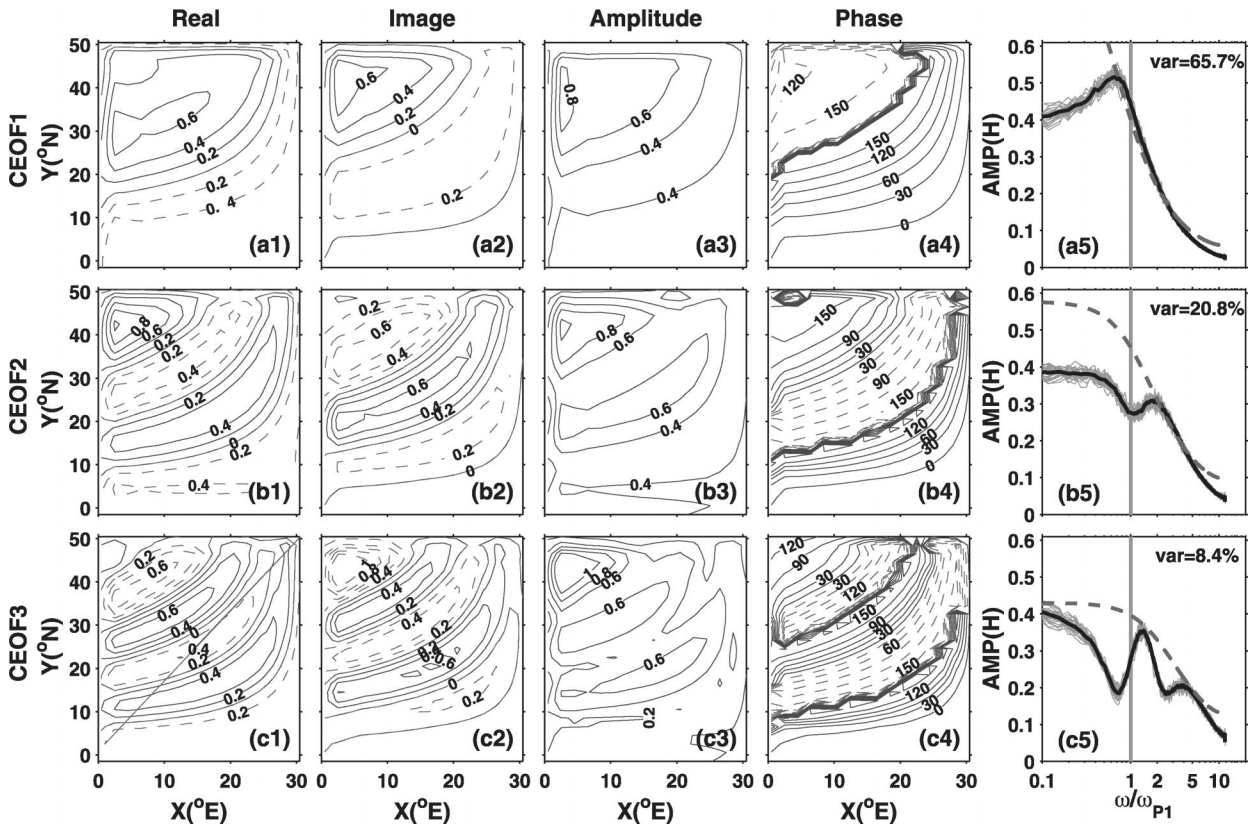

FIG. 9. The leading CEOF modes in the time-forward model forced by stochastic winds of the sine profile in Fig. 3a. (a1) Real part, (a2) imaginary part, (a3) amplitude, and (a4) phase of the CEOF1 averaged for the 25-member ensemble (virtually the same as CEOF1 in each individual member). The amplitude spectra of the temporal coefficients of the real part are drawn as thin gray lines for each member in (a5), where the heavy black line represents the average of the 25 ensemble members. (b1)–(b5) and (c1)–(c5) The same as (a1)–(a5), but for CEOF2 and CEOF3, respectively.

the 90% level only in the central equatorial region. The resonant EB and PB modes are now captured in CEOF1 (Fig. 15a) and CEOF2 (Fig. 15b), respectively. Now the pattern of CEOF1 (Figs. 15a1–15a4) resembles closely to that of the first EB mode (Cane and Moore 1981; Yang and Liu 2003), characterized by a variability amplitude trapped near the equator and a variability spectrum dominated by the first EB mode (Fig. 15a5). In comparison, the pattern of CEOF2 (Figs. 15b1–15b4) is distributed over the entire basin, with a wavenumber-1 structure along the northern boundary and a largely in-phase response along the equator. The power spectrum of the CEOF2 coefficient exhibits a significant (>90%) peak near the first PB mode (Fig. 15b5). As in the previous case of the sine wind, the CEOF modes are capable of extracting the dominant resonant peak

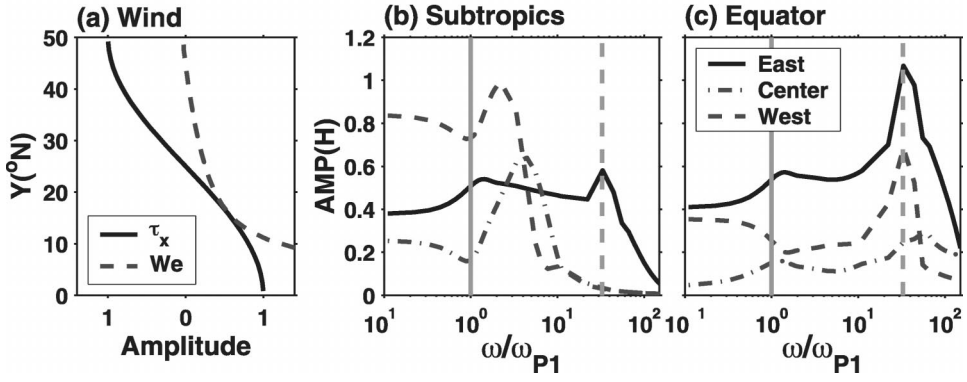

FIG. 10. The amplitude spectra in the periodic model as in Fig. 3, but for the cosine profile in (a).

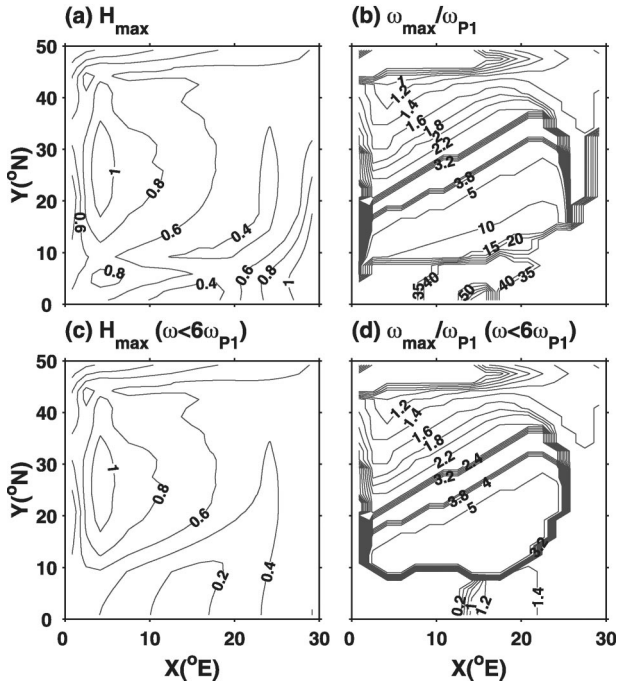

FIG. 11. (a) Magnitude and (b) frequency (normalized by ω_{P1}) at the primary peak of the power spectra in the entire frequency band forced by the white noise wind of the cosine profile in Fig. 10a in the periodic model. (c), (d) The same as (a) and (b), but for the primary peak in the low-frequency range $\omega < 6\omega_{P1}$.

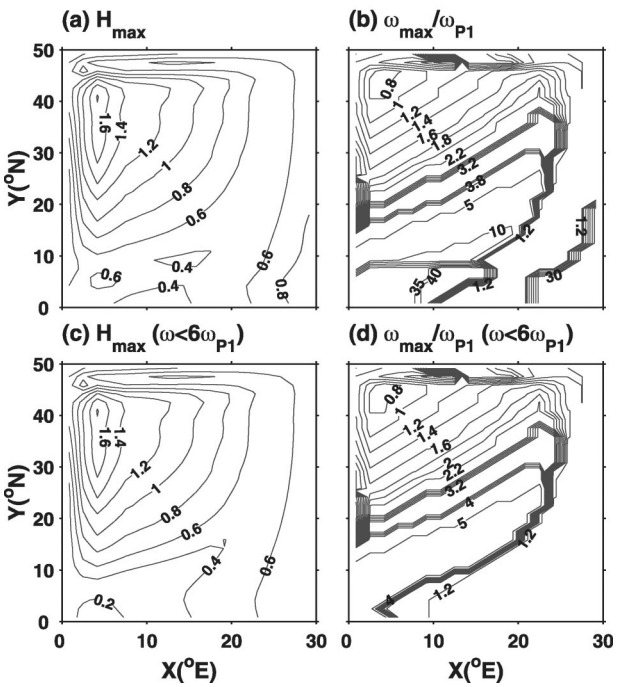

FIG. 13. The same as Fig. 11, but for the shifted cosine wind in Fig. 12a.

response and, in turn, physical modes appear more clearly than the regional time series (Fig. 14). If we perform the CEOF analysis to the low-pass data in the range of, say, $\omega < 6\omega_{P1}$,the high-frequency EB mode is largely filtered. Now, CEOF1 is dominated by the first PB mode (not shown), as expected. Therefore, the combination of low-pass filtering and CEOF analysis proves effective in extracting the resonant response of the PB mode.

6. Summary

Two linear shallow water models are solved numerically to study the response of the tropical ocean to stochastic wind forcing. Consistent with the theory (Part I), in response to an extratropical stochastic wind, the tropical ocean may exhibit decadal spectral peaks due to the resonance of the PB mode, with a rather uniform response in the equatorial and eastern boundary region. In contrast, the extratropical interior ocean is contributed to significantly by the forced response by local Ekman pumping, with the preferred spectral peak changing frequency with location. These resonant PB mode responses are robust, and can be extracted as the leading CEOF modes in the time-forward model. Our models are still very simple and idealized. The results here need to be further studied in more complex ocean models and in a more realistic setting. Nevertheless, we believe, the

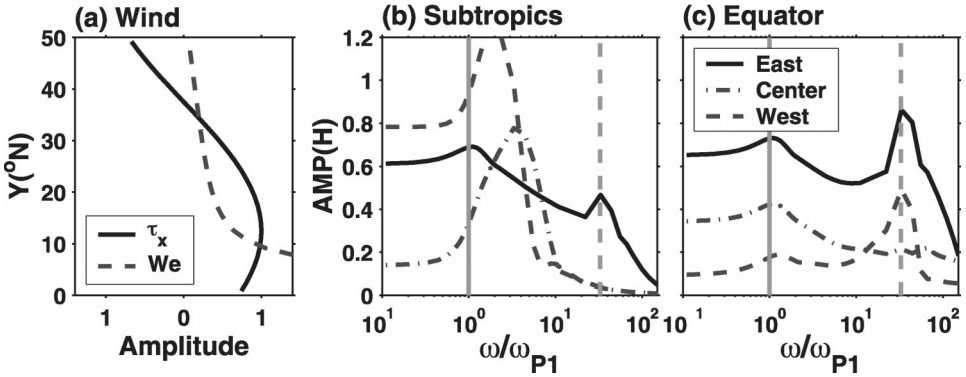

FIG. 12. The amplitude spectra in the periodic model as in Fig. 10, but for the cosine profile shifted poleward by 12°, as shown in (a).

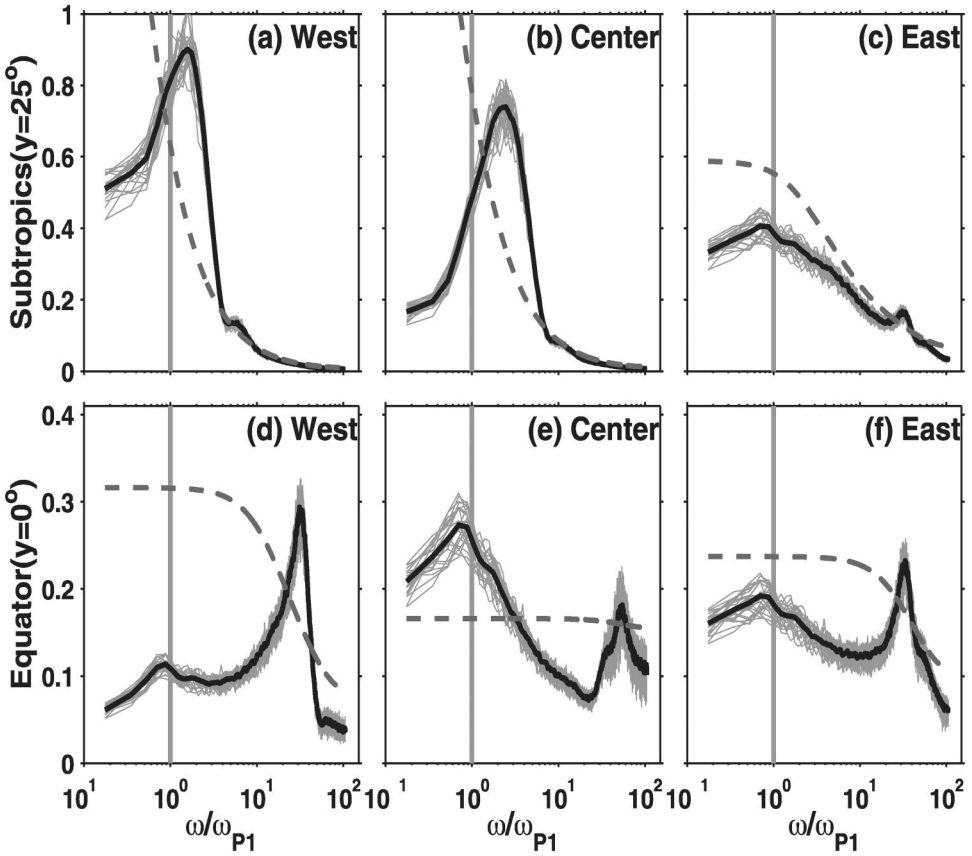

FIG. 14. Regional amplitude spectra in the time-forward model as in Fig. 6, but for the shifted cosine wind profile in Fig. 12a in a 25-member ensemble. Each member is integrated for 100 yr, with the 10-day average data used for analysis.

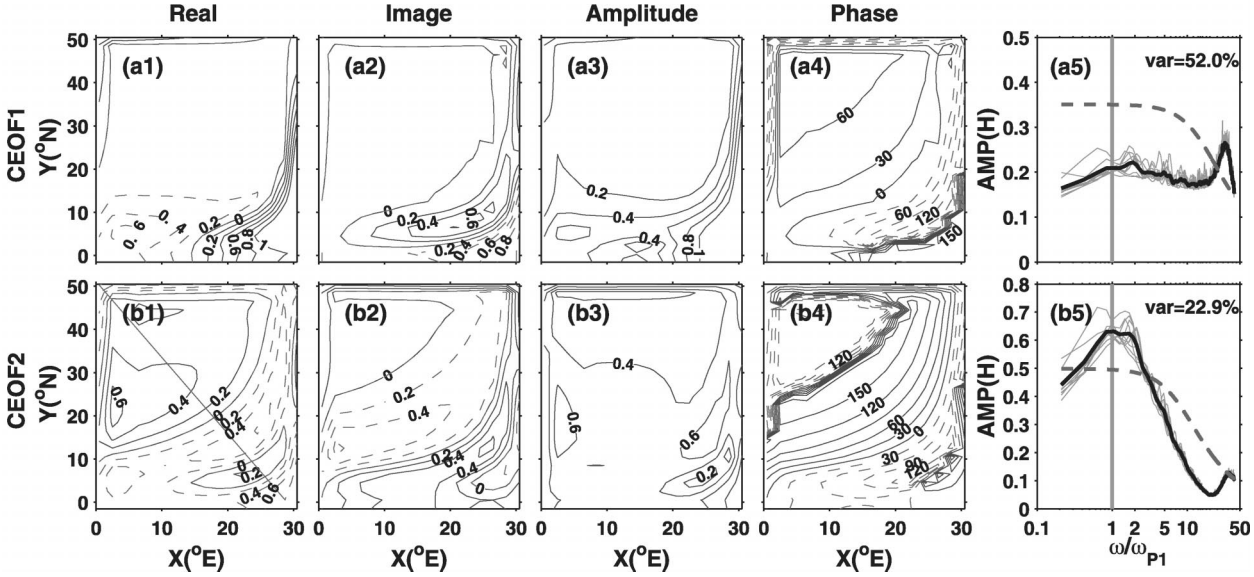

FIG. 15. The CEOF1 and CEOF2 as in Figs. 9a1–9a5 and Figs. 9b1–9b5, but for the shifted cosine wind profile in Fig. 12a derived from the same 25-member ensemble in Fig. 14.

resonance of the PB mode potentially provides a mechanism for tropical decadal oceanic variability.

Acknowledgments. This work is supported by NOAA, NASA, and DOE. We would like to thank Prof. E. DeWeaver of UW–Madison for a discussion of the construction of the stochastic forcing used in the time-forward model, Dr. Luo Jingia of Tokyo University for sharing with us his CEOF program, and two anonymous reviewers for their invaluable comments.

REFERENCES

Barnett, T., D. W. Pierce, M. Latif, D. Dommenget, and R. Saravana, 1999: Interdecadal interactions between the tropics and the midlatitudes in the Pacific basin. *Geophys. Res. Lett.,* **26,** 615–618.

Cane, M., and D. Moore, 1981: A note on low-frequency equatorial basin modes. *J. Phys. Oceanogr.,* **11,** 1578–1584.

Cessi, P., and S. Louazel, 2001: Decadal oceanic response to stochastic wind forcing. *J. Phys. Oceanogr.,* **31,** 3020–3029.

Frankignoul, C., P. Muller, and E. Zorita, 1997: A simple model of the decadal response of the ocean to stochastic wind forcing. *J. Phys. Oceanogr.,* **27,** 1533–1546.

Fu, L.-L., and D. B. Chelton, 2001: Large-scale ocean circulation. *Satellite Altimetry and Earth Sciences,* Academic Press, 133–169.

Gu, D., and S. G. H. Philander, 1997: Interdecadal climate fluctuations that depend on exchanges between the tropics and extratropics. *Science,* **275,** 805–807.

Horel, J. D., 1984: Complex principal component analysis: theory and examples. *J. Climate Appl. Meteor.,* **23,** 1660–1673.

Houghton, R. W., and Y. M. Tourre, 1992: Characteristics of low-frequency sea surface temperature fluctuations in the tropical Atlantic. *J. Climate,* **5,** 765–771.

Jin, F. F., 2001: Low-frequency modes of tropical ocean dynamics. *J. Climate,* **14,** 3874–3881.

Kleeman, R., J. P. McCreary, and B. A. Klinger, 1999: A mechanism for generating ENSO decadal variability. *Geophys. Res. Lett.,* **26,** 1743–1746.

Liu, Z., 2002: How long is the memory of tropical ocean dynamics? *J. Climate,* **15,** 3518–3522.

——, 2003: Tropical ocean decadal variability and resonance of planetary wave basin modes. Part I: Theory. *J. Climate,* **16,** 1539–1550.

North, G., 1984: Empirical orthogonal functions and normal modes. *J. Atmos. Sci.,* **41,** 879–887.

Timmermann, A., F.-F. Jin, and J. Abshagen, 2003: A nonlinear theory for El Niño bursting. *J. Atmos. Sci.,* **60,** 152–165.

Yang, H., and Z. Liu, 2003: Basin modes in a tropical–extratropical basin. *J. Phys. Oceanogr.,* **33,** 2751–2763.

Zhang, Y., M. Wallace, and D. Battisiti, 1997: ENSO-like interdecadal variability: 1900–93. *J. Climate,* **11,** 1004–1020.